Chemical Engineering Journal Advances 6 (2021) 100094

Contents lists available at ScienceDirect

Chemical Engineering Journal Advances

journal homepage: www.elsevier.com/locate/ceja

Three-dimensional reduced graphene oxide decorated with iron oxide nanoparticles as efficient active material for high performance capacitive deionization electrodes

Yolanda Belaustegui*, Inés Rincón, Francisco Fernández-Carretero, Patxi Azpiroz, Alberto García-Luís, David Alfredo Pacheco Tanaka

Parque Científico y Tecnológico de Bizkaia, TECNALIA, Basque Research and Technology Alliance (BRTA), Astondo bidea, Edif. 700, Derio, Bizkaia 48160, Spain

ARTICLE INFO

Keywords:
Graphene
Capacitive deionization desalination
Electrosorption capacity
Iron oxide nanoparticles

ABSTRACT

A three-dimensional reduced graphene oxide decorated with iron oxide nanoparticles (3D rGO-Fe_2O_3) material with a suitable porous structure was synthesised using a one-step hydrothermal process in order to fabricate novel electrodes for capacitive deionization (CDI) water desalination. The morphological and structural properties of the as-synthesised compounds were characterised by scanning electron microscopy (SEM), Brunauer-Emmett-Teller (BET), Raman spectroscopy (RS), X-ray diffraction (XRD) and thermal gravimetric analysis (TGA). The CDI electrodes were electrochemically analysed by cyclic voltammetry (CV) and electrochemical impedance spectroscopy (EIS). A maximum value of specific capacitance of 345 F g^{-1} was achieved at 5 mV s^{-1} scan rate using a NaCl 0.1 mol L^{-1} solution. The ion removal performance of the CDI electrodes was evaluated with NaCl solutions of different concentrations, showing electrosorption capacities as high as 945 mg g^{-1} for 11,700 mg L^{-1} (200 mmol L^{-1}) NaCl solutions, which substantially surpasses results of other carbon-based CDI electrodes.

1. Introduction

The growth of the inhabitants, water contamination and the consequence of climate change increase the water demand every year. The World Health Organization anticipates that by 2025, 1.8 billion people will tackle extreme fresh-water lack, signifying that efficient actions must be taken, regarding rising water supply or managing water require, to surpass this obstacle [1]. In this scenario, which the major part of the Earth´s water (about 98%) is seawater or brackish water, the desalination or salt removal technologies offer promising solutions to face this problem. Nowadays, reverse osmosis (RO), electrodialysis (ED), ion exchange (IE) and thermal processes (MSF) are extensively used for fresh-water provision [2]. Nevertheless, energy consumption and operating costs of these technologies are very high. Therefore, a lot of hard work has been devoted to developing new desalination methods using inexpensive materials, easy equipment, simple operation and small operating costs. Among them, capacitive deionization (CDI) technology is took into account as an emerging desalination technology and supposed to be one of the most hopeful technique that could satisfy all the above-mentioned requisites [3–7].

CDI is an electrochemical method for removing salt ions from salty solutions based in the electroadsorption of ions inside the porous electrodes when a small voltage (0.8 – 2.0 V) is applied to the electrodes [5]. The working principle of this method is the formation of an electrical double-layer capacitor (EDL) between the solution and the porous electrode interface. When electrodes are replete with salt ions, the cell voltage must be reversed, reduced or shorted to regenerate the electrodes, and the collected ions are discharged into a wastewater solution generating a concentrated salt stream. One of the greatest benefits of this technology is its high hypothetical energy efficiency for desalination. As an example, the inherent energy necessity by reverse osmosis, the most effective desalination technique currently available, for brackish water is ≈ 1 kWh m^{-3}, which is much higher to that of CDI (≈ 0.1 kWh m^{-3}) [5]. Other remarkable advantages are: (1) low equipment and operational costs due to it does not need high-pressure; (2) due to it works in low voltage, it can be easily connected with solar/wind power to run in isolated areas where the access to the electricity is a big problem; (3) the recovery of water is higher compared to other desalination techniques such as RO; (4) the application range is large because CDI electrodes can resist much higher temperature than polymeric membranes in RO;

* Corresponding author.
E-mail address: yolanda.belaustegui@tecnalia.com (Y. Belaustegui).

https://doi.org/10.1016/j.ceja.2021.100094
Received 22 October 2020; Received in revised form 12 January 2021; Accepted 13 January 2021

and (5) finally, the CDI cell is able to high-energy recovery because it works like a capacitor [8].

CDI was conceived in 1960 [9], however, CDI based desalination technique has not reached the full water market potential due mainly to the scarcity of appropriate electrode materials with high salt adsorption capacity (SAC) and high average salt adsorption rate (ASAR). In theory, a suitable electrode material for CDI should posse high electrical conductivity, elevated surface area, high porosity, electrochemical stability, fast adsorption-desorption kinetic, good wetting behaviour, low cost and scalability [10,11]. Usually, carbon materials with elevated electrical conductivity and structures with adjustable characteristics have been contemplated as encouraging electrode materials for CDI [12,13]. The literature reports a lot of carbon materials including graphene [14], carbon nanofibers [15], carbon nanotubes [16], activated carbons [17], carbon aerogels [18] and combinations of them [19,20]. Nonetheless, the NaCl adsorption capacity of these materials is inferior than the supposed estimations [12]. Besides, for most of them, the manufacturing processes are relatively complex and high making cost.

The electrosorption performance is improved with high specific surface area electrode materials but the proper pore size distribution and the connectivity of the pores of the electrodes are even more critical factors [21]. The different size of the pores/holes in CDI electrodes has different functions. Micropores enhance the EDL capacitance and as consequence, improve the CDI performance; however, the pore size reduction lead to strongly overlap of the double layers and confinement effect intensifies the deformation of EDL formation within micropores which is hazardous for the CDI performance [22]. Mesopores supply expanded efficacious surface area and the adequate pore/hole size dispensation for electrode materials, which can make easier ions movement to achieve high electrosorption capacity. Finally, the macropores can cut down the diffusion spaces for salt ions to inward pores [23].

Graphene is a strong two-dimensional (2D) sheet of sp^2-hybridized carbon which possess the properties of exceptional electronic conductivity, elevated specific surface area, adjustable functionalization and great chemical and electrochemical stability. In addition, graphene oxides sheets can easily self-assemble into 3D networks with macroporous structure exhibiting a high surface area with a favourable pore size distribution including mesopores and micropores [14], in contrast to other amorphous or one dimensional (1D) carbon materials. This structure presents many reachable open pores to NaCl ions and allows for the growth and fixing of functional inorganic nanomaterials with high charging quantity. The addition of metal oxide nanoparticles such as TiO_2, ZnO, Fe_2O_3 and MnO_2 on graphene electrodes impede the aggregation tendency which can notably enhance the specific capacitance [24,25]. As a consequence, CDI desalination efficiency can be made better due to the replacement of suitable physicochemical properties of graphene as elevated hydrophilicity to rise the wetting of the electrode, inhibition of physical adsorption of ion species altering electroadsorption/desorption capacity during CDI operation [26-28], or modifying the surface zeta-potential on the graphene electrode to rise the ion elimination amount [29]. Among the transition metal oxides, due to its low cost and environmental impact, iron oxide is one of the more favourable material.

There are several methods to carry out the synthesis of graphene-metal oxide composites such as ultrasonic spray pyrolysis [30], hydrothermal [31], solvothermal [32] and microwave-assisted reduction [33,34]. Among them, the hydrothermal process allows the easy synthesis of 3D graphene materials at low cost with a controlled structure [14,31].

In this work, an easy and versatile hydrothermal method to synthesise a new material based on graphene 3D decorated with iron oxide nanoparticles, for the use in the preparation of CDI electrodes is presented. The chemical synthesis involves the formation of iron oxide nanoparticles and the reduction of graphene oxide (GO) in one single step, followed by a freeze-drying treatment. The electrosorption capacity of the electrodes in desalination is evaluated and the effect of the iron oxide nanoparticles addition to the 3D reduced graphene oxide structure is investigated.

Table 1
Experimental conditions for the preparation of GO samples by hydrothermal treatment.

Sample code	[GO] (mg mL^{-1})	Metal Salt	[MOx] (mmol L^{-1})	pH
3D rGO	4	—	—	9
3D rGO-Fe_2O_3	4	$FeSO_4.7H_2O$	0.5	9

2. Experimental

2.1. Synthesis of 3D rGO-Fe_2O_3

Commercial graphene oxide (GO) dispersion (4 mg mL^{-1}) supplied by Graphenea (average particle < 10 μm; carbon: 49–56%; oxygen: 41–50%; nitrogen: 0–1%) and ferrous sulphate heptahydrate ($FeSO_4.7H_2O$) were used as starting materials for the preparation of the samples.

25 g GO in water suspension with a 4 mg/mL concentration, an aqueous solution of $FeSO_4.7H_2O$ 0.5 mmol L^{-1} in a weight ratio of 1:0.6 (GO:$FeSO_4.7H_2O$) and NH_4OH (25%) to adjust the pH to 9 were loaded into a Teflon lined stainless steel autoclave and warned up at 180 ºC for 16 h. The synthetized material was cleaned three times with deionized water and frozen for 24 h at -80 ºC. Then it was freeze-dried at -10 ºC, 63 Pa for 12 h. For comparison, a sample of rGO was synthesized using the same method. **Table 1** presents the parameters used for the preparation of GO materials.

2.2. Sample characterisation

A combining of supplementary techniques was used to characterize the as-synthesized materials. The morphology was examined by scanning electron microscopy (SEM, Quanta FEG 250). The phase and crystallinity were researched using XRD (Bruker D8 Advanced X-Ray diffractometer). The porosity measures were performed using a gas adsorption-desorption equipment (ASAP 2010 Micromeritics). The Brunauer-Emmet-Teller (BET) surface area and pore size distribution were determinate quantifying the adsorbed gas quantity to produce a monolayer on the solid surface. t-plot method was used to calculate the micropores volume and the mesopores was obtained by difference. In order to estimate the volume distribution of mesopores, Barrett, Joyner and Halenda (BJH) method was utilised. The distribution of macropores was evaluated by mercury intrusion porosimetry (Micromeritics Autopore IV 9500). Raman spectra (RS) was obtained with a Renishaw in Via Raman microscope with a laser wavelength of 488 nm and spot size of 0.5 nm. The thermal stability of the materials was determined by thermal gravimetric analysis (TGA, Setaram TG-DTA92) using a heating rate of 3 ºC/min under dry air. The contact angle was measured with Goniometer GBX Digidrop contact angle meter.

2.3. CDI electrode preparing and electrochemical testing

2.3.1. Preparing of 3D rGO and 3D rGO-Fe_2O_3 electrodes

3D rGO and 3D rGO-Fe_2O_3 electrodes were prepared by blending the as-synthesised graphene material with polyvinyl alcohol and ethanol. The blend was agitated by ultrasonication for merely 8 h to ensure homogeneity. This graphene slurry was deposited onto a graphite sheet (Mersen Ibérica), which acted as current collector, and dried in an oven

at 60 °C to remove the organic solvents and to obtain a plane electrode.

Electrodes of 2 cm^2 for the electrochemical testing and 9 cm^2 for the CDI experiments were utilized.

Before their testing in the electrosorption experiments, the electrodes were conditioned by immersion in 0.1 mol L^{-1} NaCl solution for not less than 24 h to moisten the pores of the electrodes [35]. Finally, they were assembled in the CDI stack and washed with deionized water circulation to remove the probably physically adsorbed ions.

2.3.2. Electrochemical capacitive measurements

The electrochemical capacitive performance and the electrical double layer (EDL) formation were evaluated by cyclic voltammetry (CV) and electrochemical impedance spectroscopy (EIS) techniques. CV measurements were performed at room temperature with an AUTOLAB PGSTAT128N potentiostat, using a conventional three electrode configuration. The working electrode was the as-synthesized CDI electrode (2 cm^2 area), the counter electrode was a graphite rod and the reference electrode a standard Ag/AgCl electrode.

CV measurements were done in 0.1 mol L^{-1} NaCl solution with sweep rates from 5 to 100 mV s^{-1} in the potential range of -1 to 0.5 V. To calculate the specific capacitance values of the electrodes the current-voltage curves according to the Eq. 1 were taking into consideration:

$$C = \frac{1}{\upsilon m} \frac{\int_{E_1}^{E_2} I dV}{V} \quad (1)$$

where C (F g^{-1}) is the specific capacitance, v (V s^{-1}) is the potential scan rate, m (g) is the dry mass of the materials in the electrode I (A) is the response current, E_1 and E_2 (V) are the potentials in the potential window, and V (V) is the potential.

The interior resistance of the electrodes was determined by EIS analyses. The experiments were conducted with an AUTOLAB PGSTAT128N potentiostat utilizing the three electrodes cell. Alternating voltage amplitude was 0.01 V close to the equilibrium potential (0 V) and the information was gathered from 10,000 Hz to 0.1 Hz frequency range.

2.4. Electrosorption experiments of CDI electrodes

The electrosorption capacity of the 3D rGO and 3D rGO-Fe_2O_3 electrodes were carried out by batch mode experiments in a continuously recirculating system. The experimental set-up was composed of a CDI symmetric electrosorption cell, two tanks (one for feed solution and another to pick up the treated solution), a conductivity meter (Hanna Microprocessor Conductivity/TDS meter), a peristaltic pump (Fisher Scientific, Mini-pump variable flow), and a power supply (DC Lab Power supply LABPS1503). In turn, CDI unit cell is made up of two electrodes films of 9 cm^2 area placed in parallel and isolated by a nylon spacer to avoid electrical shortcut and to let water to circulate throughout the electrodes. The flow rate was set to 7.7 mL min^{-1}. A voltage of 1.2 V was applied to the cell and kept on as far as its charging was full, and the concentration of the salt remained constant through the cell. Experiments were conducted at room temperature with NaCl solutions with different concentrations between 11,700 and 585 mg L^{-1} with a total volume of 100 mL. The conductivity of the treated water was continually screened and transformed to the sodium concentration value achieved by a calibration procedure using the linear relationship between salt concentration, [NaCl] (mg L^{-1}) and the conductivity of the solution, σ (μS cm^{-1}),

$$[\mathrm{NaCl}] = 0.5539\,\sigma \quad (2)$$

The salt adsorption capacity SAC (mg g^{-1}) of the CDI electrodes was obtained using the next equation:

$$\mathrm{SAC} = \frac{(C_o - C_t)\,V}{C_o} \cdot 100 \quad (3)$$

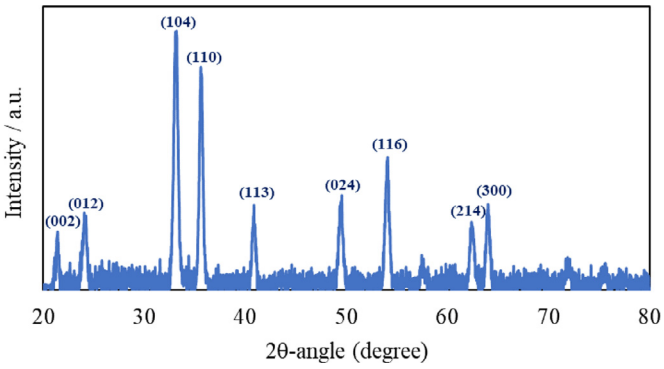

Fig. 1. X-Ray diffraction patterns of 3D rGO-Fe_2O_3.

where, C_o (mg L^{-1}) was the initial concentration, C_t (mg L^{-1}) was the concentration at time t (min) in equilibrium, V (L) was the solution volume and m (g) was the total mass of the two electrodes. The reproducibility was checked carrying out several experiments on 3D rGO and 3D rGO-Fe_2O_3 materials, and the corresponding SAC was calculated doing the average of the results achieved in these experiments.

3. Results and discussion

3.1. Physicochemical properties of 3D rGO and 3D rGO-Fe_2O_3

3D rGO-Fe_2O_3 material with 3D interconnected reduced graphene oxide networks and embedded Fe_2O_3 nanoparticles as well as 3D rGO were obtained by hydrothermal process followed by a freeze-drying treatment. Hydrothermal process combined the growth of iron oxide nanoparticles and the reduction of graphene oxide (GO) in one unique stage while the porous structure was formed through the freezing process via the ice crystals.

Fig. 1 depicts XRD pattern of 3D rGO-Fe_2O_3 material. The diffraction peaks observed in the XRD pattern are around 21.4º, 24.2º, 33.2º, 35.6º, 40.8º, 49.1º, 54.1º, 62.5º and 63.9º. All of peaks, excepting 21.4º which is characteristic of reduced graphene oxide (rGO) [36], matched with the standard hematite sample (α-Fe_2O_3, JCPDS Card No. 33–0664). These reflections correspond to (002) for rGO and to (012), (104), (110), (113), (024), (116), (214) and (300) for hematite, which prove that the iron oxide nanoparticles in the sample were rhombohedral crystalline hematite (α-Fe_2O_3). The peak at 21.4º confirmed the GO reduction during the hydrothermal process.

SEM images of 3D rGO-Fe_2O_3 sample are presented in Fig. 2. The micrographs show a macroporous 3D structure with open pores. Higher magnification SEM (Fig. 2**d**) reveals a homogenous distribution of Fe_2O_3 nanoparticles with a particle dimension varying from 20 to 30 nm along the rGO layers. These results confirmed that rGO is adequate as support material for the growth of Fe_2O_3 nanoparticles, which prevents the stacking of graphene sheets and leaving large void space of pores. This porous structure contributes to a fast electrolyte access and the totally contact between electrodes and electrolyte as proposed Ma et al. [37]. That is, from a macrostructural point of view, the main advantage of introducing Fe_2O_3 nanoparticles was to separate the graphene adjacent layers and to inhibit sheet aggregation.

The thermogravimetric analysis of 3D rGO-Fe_2O_3 and 3D rGO were performed in air atmosphere to estimate the thermal stability of the as-synthesized samples. In Fig. 3 the TGA curves (Fig. 3**a**) and the derivative curves (Fig. 3**b**) of 3D rGO-Fe_2O_3 and 3D rGO are presented showing significative differences in mass loss. In the case of 3D rGO-Fe_2O_3 there is a weight loss below 415ºC which corresponds to the evaporation of absorbed water and the decomposition of oxygen groups (mainly carboxylic). From 415 to 520 C two distinctive peaks are observed prob-

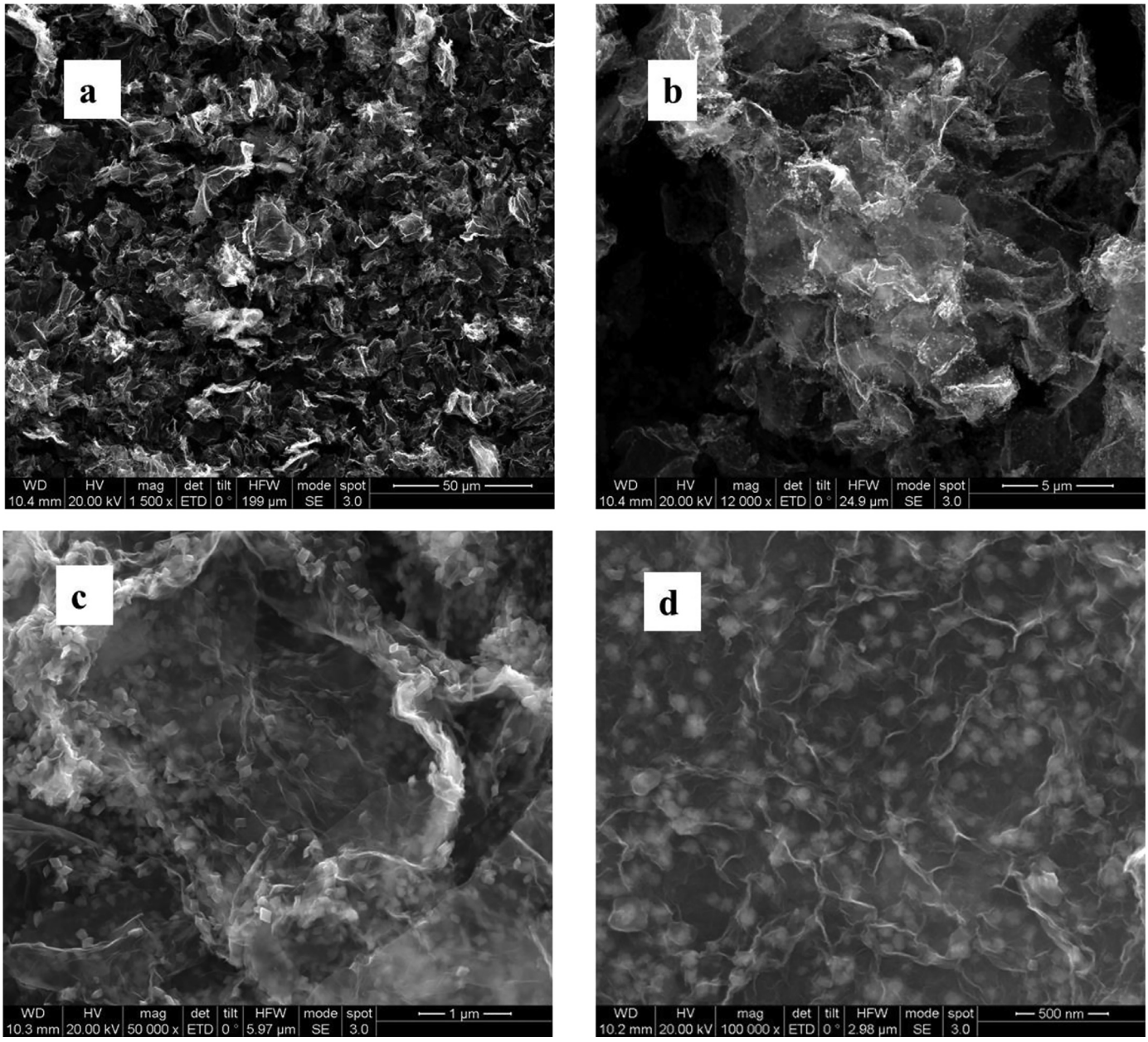

Fig. 2. SEM images of 3D rGO-Fe_2O_3 at various magnifications.

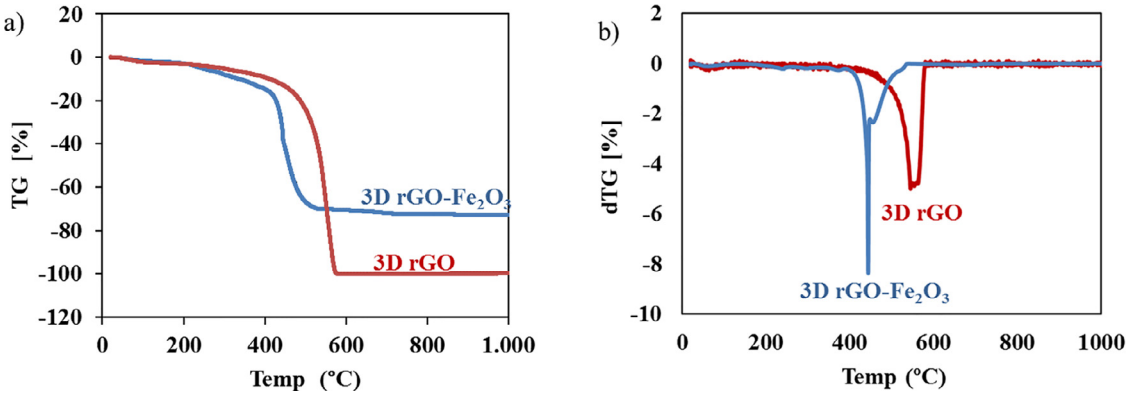

Fig. 3. Thermogravimetric curves of 3D rGO-Fe_2O_3 and 3D rGO materials.

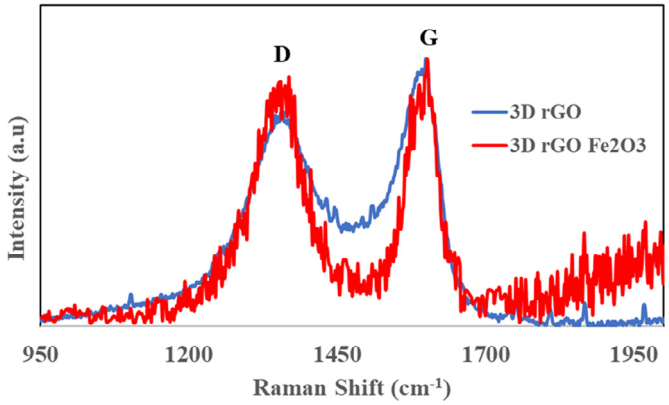

Fig. 4. Raman spectra of rGO and 3D rGO-Fe_2O_3 nanomaterials. The spectra are normalised for an easier comparison.

ably from the decomposition of GO with and without Fe_2O_3. From 500 to around 800 ºC the small weight lost indicates the removal of water from Fe_2O_3 product of the sintering. This weight loss could be attributed to water produced from the condensation of Fe-OH + HO-Fe giving Fe-O-Fe+H_2O, or by O_2 from the decomposition of Fe_2O_3 [38]. After 800 ºC, the curve becomes parallel to the temperature axis indicating that a stable Fe_2O_3 is formed, which representing around 19% of the total weight of the sample. The decomposition of 3D rGO-Fe_2O_3 is produced at lower temperatures than 3D rGO due to effect of the interaction of Fe_2O_3 with GO and indicating a lower reduction of GO. This fact suggests that the presence of Fe_2O_3 nanoparticles favours the existence of more oxygen containing groups in 3D rGO-Fe_2O_3 material, leading also to an increase of its hydrophilic character which is advantageous to obtain a good contact between the water and electrode material.

The reduction of graphene oxide was examined by Raman spectroscopy. Usually, D and G bands, which are characteristics of defects and single graphitic layer existence on graphitic material, represent sp^3 and sp^2 bonded carbon structures, respectively [39]. The structural disorder in carbon materials can be evaluated by the intensity ratio of D to G band (I_D/I_G). As shown in **Fig. 4**, both samples, 3D rGO and 3D rGO-Fe_2O_3, have these two bands, D band (1350 cm^{-1}) and G band (1580 cm^{-1}). Nevertheless, 3D rGO-Fe_2O_3 shows a more intense D band than 3D rGO, with an I_D/I_G ratio of 0.99 versus 0.80, respectively. This higher I_D/I_G ratio implied that the iron oxide nanoparticles incorporated in 3D rGO-Fe_2O_3 induced structural defects and distortion in the rGO network. This is a significant property due to the existence of defects can produce more approachable surface area and origin an augment in the ability to collect charges, which is positive for the charge transfer in the adsorption process [40].

The porous structure of 3D rGO and 3D rGO-Fe_2O_3 materials, as well as their pore size distribution were determinate by N_2 adsorption-desorption isotherms. **Fig. 5** presents the BET analysis of both materials. As shown in **Fig. 5a** and **5c**, the isotherms exhibit a standard type IV behaviour, with the existence of a hysteresis slope at higher relative pressures, which indicated the presence of mesoporosity and macroporosity [41]. In the case of 3D rGO-Fe_2O_3, the specific surface area was 212 m^2 g^{-1} and the micropore volume 9.23 mm^3 g^{-1}. For 3D rGO the specific surface area was 207 m^2 g^{-1} and the micropore volume was 21.6 mm^3 g^{-1}. The surface area of both materials is similar, however, the micropore volume of 3D rGO is higher than 3D rGO-Fe_2O_3 indicating a major presence of macropores and mesopores in 3D rGO-Fe_2O_3.

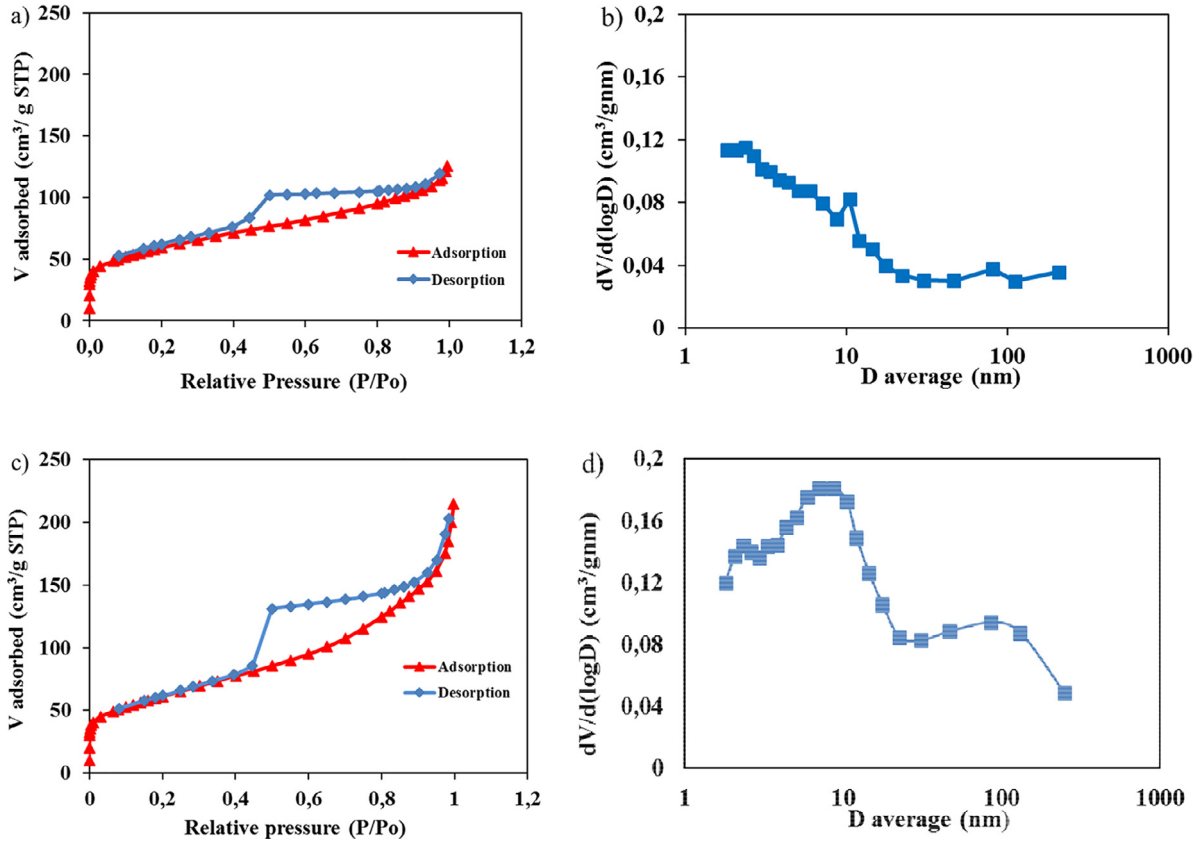

Fig. 5. BET analysis for 3D rGO and 3D rGO-Fe_2O_3 a) N_2 adsorption-desorption isotherm for 3D rGO, b) Pore size distribution for 3D rGO, c) N_2 adsorption-desorption isotherm for 3D rGO-Fe_2O_3, b) Pore size distribution for 3D rGO-Fe_2O_3.

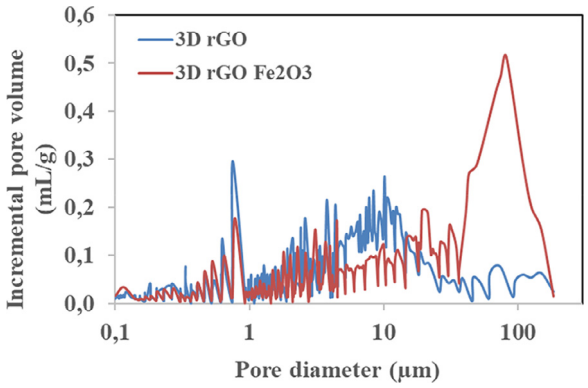

Fig. 6. Mercury intrusion porosity analysis for 3D rGO and 3D rGO-Fe_2O_3.

If the pore size distribution of the samples was compared (**Fig. 5b** and **5d**) it came out that 3D rGO-Fe_2O_3 comprises a considerable portion of mesopores (2–50 nm) and macropores (>50 nm) than 3D rGO; which is supposed to be optimum for electrosorption in CDI process [7], since micropores (< 2 nm) contributed to enhance the specific surface area of the electrodes, but are hardly accessible for the ions and resulting in lower CDI-active specific surface area [42]. In addition, in order to obtain more information of the macroporosity, mercury intrusion analysis was performed. As shown in Fig. 6, until 5 μm the porosity of the both samples was quite similar. However, 3D rGO showed a porous distribution centred in 10 μm whereas in the case of 3D rGO-Fe_2O_3 was around 100 μm, confirming that 3D rGO-Fe_2O_3 had higher macropores than 3D rGO.

These results reveal the increase in mesoporosity and macroporosity of 3D rGOFe_2O_3 electrode with the introduction of iron oxide nanoparticles on graphene oxide sheets. In accordance with the data obtained for Tsoncheva et al. [43], it could be ascribed to the deposition of the iron particles onto the graphene structure that occurred in a higher degree on the external surface of the graphene host matrix, increasing surface area and the appropriate pore/hole size distribution.

3.2. Electrochemical analysis

Fig. 7 shows the CV performances of 3D rGO and 3D rGO-Fe_2O_3 electrodes in 0.1 M NaCl at different scan rates from 5 mV s^{-1} up to 100 mV s^{-1} in the potential range of -1 to 0.5 V vs Ag/AgCl. The CV curves depict a quasi-rectangular shape in the scanned voltage range without any obvious redox peaks, suggesting a clear capacitive behaviour because the perfect electrical double-layer (EDL) formation at the electrode-solution interface. When the scan rate raised a slight deviation from a rectangular to an oval shape was observed.

The specific capacitances were estimated from current voltage cycles in accordance with Eq. (1). These results showed that, with the decreased of scan rate, the specific capacitance of 3D rGO and 3D rGO-Fe_2O_3 dramatically increased from 36.19 to 198.11 F g^{-1} and from 74.63 to 345.13 F g^{-1} for 100 mV s^{-1} and 5 mV s^{-1}, respectively, which represents an increase of 40% in capacity when Fe_2O_3 is present. As general tendency, the value of capacitance decreases when rising the scan rate (mV s^{-1}). Working at small scanning rates, the salt ions get sufficiently time to diffuse into the interior pores of the electrodes, which is crucial for the formation of the EDL, consequently, the surface of the graphene electrodes are charged with more ions. In the case of increasing the scanning rate, the salt ions haven´t enough time for moving and accumulating into the inner pores. Therefore, the accessible area is reduced and the formation of EDL was incomplete.

The higher capacitance of rGO-Fe_2O_3 electrode can be due to the intercalation of iron oxide nanoparticles amongst the graphene oxide sheets that make the wettability and the hydrophilicity of the electrodes as well as the mesoporosity better, allowing higher ion accessibility and the possibility to gather a great quantity of the salt ions on the electrode surface. Besides, as demonstrated by TGA analysis, 3D rGO was more reduced than 3D rGO-Fe_2O_3 and as consequence, 3D rGO-Fe_2O_3 had more presence of hydrophilic groups on the graphene surface. This fact was further confirmed by water angle contact measurements of both materials (**Fig. 8**). The water angle contact for 3D rGO Fe_2O_3 is 7.7º much lower than that measured for 3D rGO of 41.4º. This indicates a better wettability and hydrophilic character for the 3D rGO Fe_2O_3 material.

As it is well-known, the wettability of the electrode affects strongly not only on the effective electrode area utilised for electrosorption but also on the diffusion kinetics within the micro/meso and macropores [44]; and it is principally influenced by the existence of functional groups on the graphene surface, such as, oxygen groups [45]. In accordance with Seo et al. [46], the capillary phenomenon reliable for the good wettability of the different materials is affected by the presence of hydrophilic groups on the graphene surface, such as carboxyl, carbonyl, and hydroxyl. The hydrophilic nature of iron oxide nanoparticles let having OH^- groups on their surface that interacts with Na^+ and Cl^- ions. OH^- groups can be protonated or deprotonated by varying the pH. Also, the incorporation of iron oxide nanoparticles in the 3D rGO improves its specific capacitance properties due to an improvement of the contact area and so a decreased interfacial resistance. **Fig. 9** depicts the CV curves of 3D rGO and 3D rGO- Fe_2O_3 at a sweep rate of 5 mV s^{-1} showing a clear enhancement in the capacitive performance of 3D rGO material when decorated with iron oxide nanoparticles.

The capacitive behaviour and the internal resistance of the electrodes material were evaluated by electrochemical impedance spectroscopy (EIS) technique. For that, the real and imaginary part of the total impedance was recorded as a function of the frequency of the input signal [47]. The Nyquist impedance graphics for the 3D rGO and 3D rGO-Fe_2O_3 based electrodes from EIS measurements carried out in Na Cl aqueous solution 0.1 M in the frequency range from 0.1 Hz to 10 kHz are displayed in **Fig. 10**. These plots show similar shapes involving two contributions. The Warburg impedance which is observed at low frequency region, is represented by a straight spike line (with comparative slopes of 45º), which is dependent on the adsorption of ions over the electrode surface and on the kinetics of the ion diffusion in solution [48]. At high-frequency region there is a small quasi-semicircle corresponding to a parallel combination of the double-layer capacitance and the charge-transfer resistance [49], as a result of the connection between the current collector and the electrode and the resistance of the porous electrode itself [48]. The equivalent circuit used for fitting the data is shown in the inset of the **Fig. 10** while the fit parameters are shown in Table 2. The bulk solution resistance, Rs can be obtained from the intercept of the high frequency semicircle with the real axis. As pointed Han et al. [50], it represents the ionic resistance of salty water, the intrinsic resistance of electrodes and the contact resistance at the interface of active material/current collectors.

In the case of 3D rGO-Fe_2O_3, the size of this high frequency semicircle, which growth as the hindrance for ions´ entry to the pores improves [51], is smaller than 3D rGO electrode, indicating that iron oxide nanoparticles introduction in graphene should be advantageous to reduce the charge transfer resistance on the electrode. The electrolyte entrance turned into simpler for the bigger pores and more difficult for the smallest pores. In this way, lower resistance relates to better electrolyte pore accessibility [48]. This result could be attributed to the increase in wettability when the iron oxide nanoparticles are incorporated. The high wettability for the 3D rGO-Fe_2O_3 makes the adhesion better thereby reducing the interfacial resistance while the more hydrophobic surface for the 3D rGO electrode lead to high electron transfer resistance due to the weak adherence between the electrolyte and the electrode surface. Keeping in mind the lower resistance and higher specific surface area, the 3D rGO-Fe_2O_3 electrode showed excellent potential for CDI application.

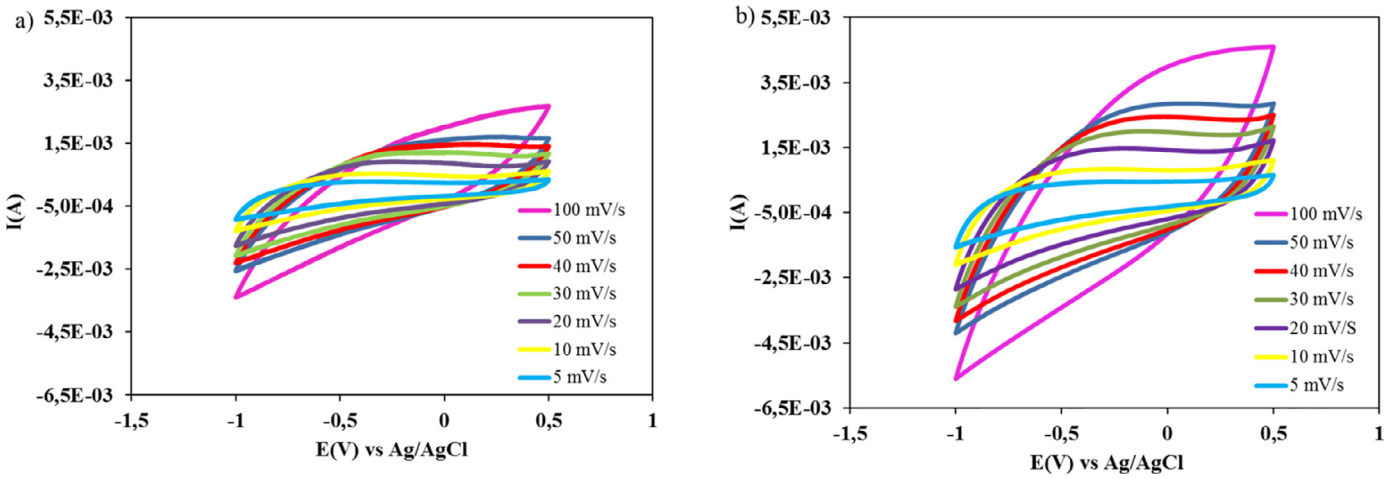

Fig. 7. Cyclic voltammograms of a) 3D rGO and b) 3D rGO-Fe_2O_3 based electrodes.

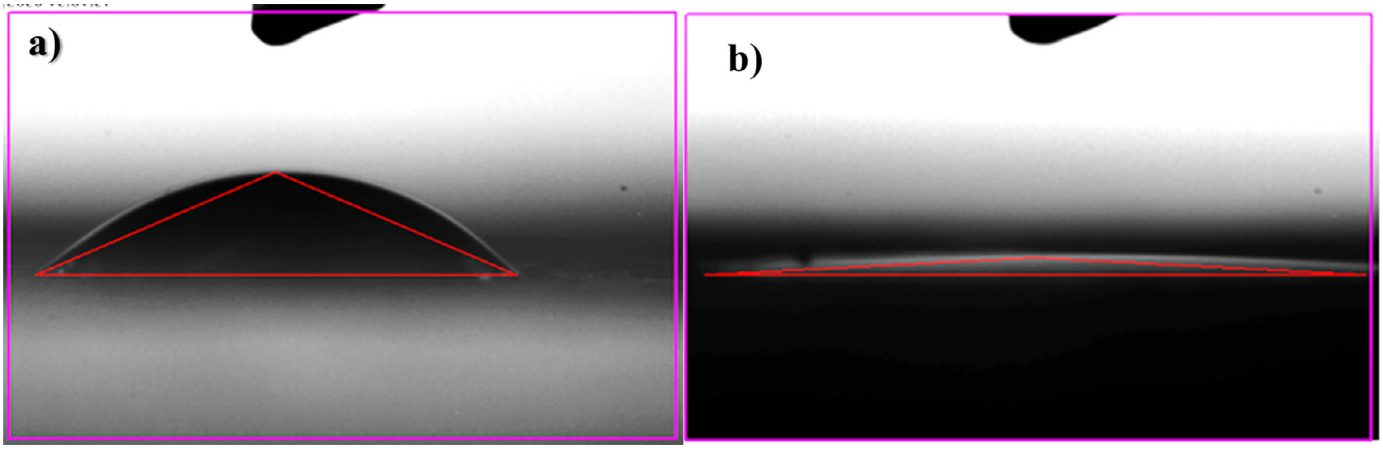

Fig. 8. Water contact angle of a) 3D rGO and b) 3D rGO-Fe_2O_3 surfaces.

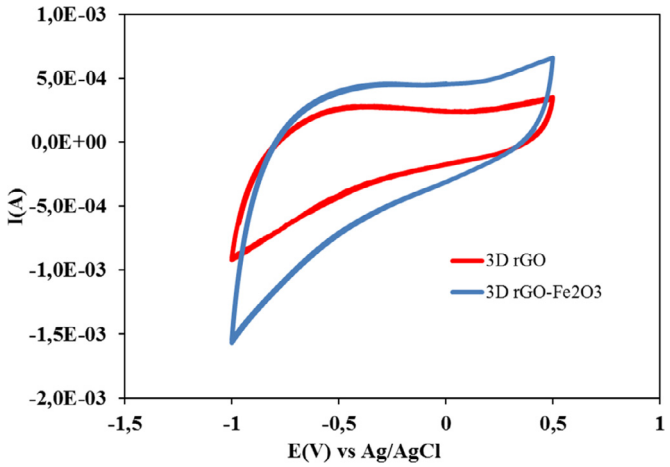

Fig. 9. Cyclic voltammograms of 3D rGO and 3D rGO-Fe_2O_3 based electrodes at 5 mV s^{-1} scan rate.

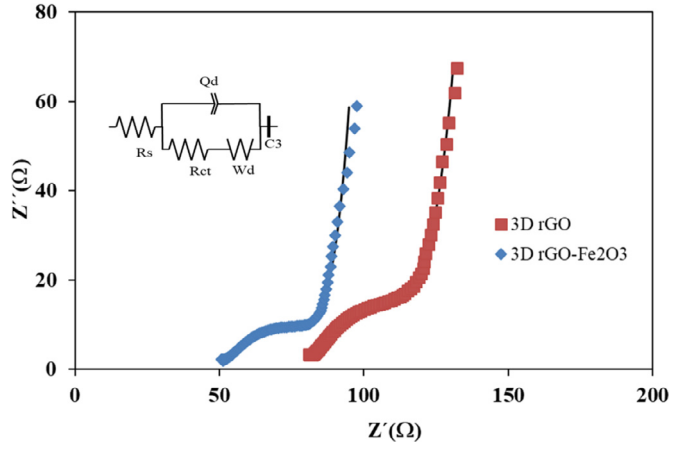

Fig. 10. Nyquist impedance plots for 3D rGO and 3D rGO-Fe_2O_3 electrodes. Inset: Equivalent circuit.

Table 2
Fit parameters of the equivalent circuit.

	Rs (Ohm)	Qd ($F•s^{nd-1}$)	nd	R_{CT} (Ohm)	S_d ($Ohms^{-1/2}$)	C3 (F)
3D rGO	80.28	3.13×10^{-3}	0.60	45.09	9.51	3.09×10^{-2}
3D rGO- Fe_2O_3	49.90	3.00×10^{-3}	0.49	41.25	7.26	3.35×10^{-2}

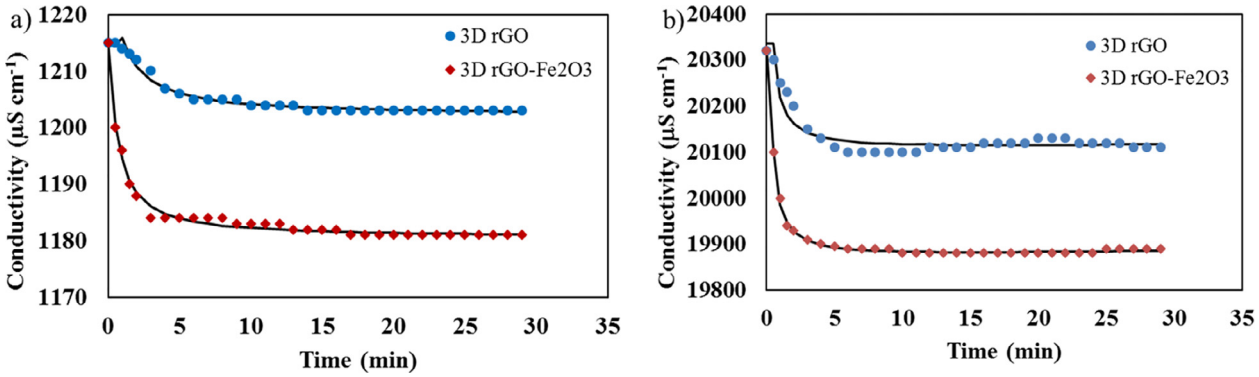

Fig. 11. Desalination performance of 3D rGO and 3D rGO-Fe_2O_3 electrodes with a) 585 mgL^{-1} and b) 11,700 mgL^{-1} NaCl solutions.

3.3. Desalination performance of the fabricated electrodes

The desalination performance of the as synthesised electrodes was measured in a batch-mode CDI pilot plant in a continuously flowing system. The total mass of the electrodes was precisely measured to estimate their SAC. The mass values measured varying between 20 and 50 mg. For each type of electrode material (3D rGO and 3D rGO-Fe_2O_3) different experiments were performed in order to verify the reproducibility, and the pertinent SAC values was calculated considering the medium value of all experiments. The electrosorption capacity of the electrodes was evaluated at several initial concentrations of NaCl solutions and the concentration variation of the NaCl was registered by a conductivity meter just at the outlet of the CDI cell where the solution left the cell. When the potential was applied, Na^+ and Cl^- ions were adsorbed over the surface of the contrarily charged electrodes producing a decreasing in the conductivity of the NaCl solution, as exhibited in Fig. 11. In the beginning of the process a quick decrease in the conductivity took place, when the concentration of the saline solution in the CDI cell experienced a considerable variation, manifesting fast adsorption of the ions. Inversely, in the next stage, the modification of the conductivity was slower until the adsorption equilibrium was achieved because the electrosorption saturation. Fig. 11 compares the desalination performance of 3D rGO and 3D rGO-Fe_2O_3 electrodes in 585 mg L^{-1} (10 mmol L^{-1}) and 11,700 mg L^{-1} (200 mmol L^{-1}) NaCl solutions. It is obvious that the desalination performance of the 3D rGO-Fe_2O_3 electrode is higher than that of 3D rGO electrode, for example, for 585 mg L^{-1}, 3D rGO-Fe_2O_3 electrodes are able to remove 74.73 mg g^{-1} while 3D rGO is able to remove only 30.77 mg g^{-1}. This result can be associated to the hydroxylation of Fe_2O_3 surface which increases the interaction with Na^+ and Cl^- ions. No pH variation or bubble formation were observed for the duration of the experiments. The SAC value of the electrodes was determined via Eq. (3). The concentration of NaCl was calculated via Eq. (2) by transforming the measured conductivity. Fig. 12 compares the electrosorption capacity of 3D rGO and 3D rGO-Fe_2O_3 electrodes at different NaCl concentrations. As a common tendency, the electrosorption capacity little by little rises with increasing NaCl concentration, under constant voltage, showing that the concentration has a beneficial effect on electrosorption performance of the electrodes. This is resulting from the better mass transfer rate of ions insides the pores and diminished EDL overlapping effects, since double-layer thickness is inversely proportional to the solution concentration. Furthermore, with the concentration increasing from 585 mg L^{-1} to 11,700 mg L^{-1}, the electrosorption capacity raise from 30.77 mg g^{-1} to 538 mg g^{-1} for 3D rGO electrodes and from 74.73 mg g^{-1} to 945 mg g^{-1} for 3D rGO-Fe_2O_3 electrodes. The comparison with the literature review (Table 3) confirms that these values are well above those recently reported for carbon-based electrode materials. The incorporation of iron oxide nanoparticles in the 3D rGO-Fe_2O_3 compound led to a higher electrosorption capacity

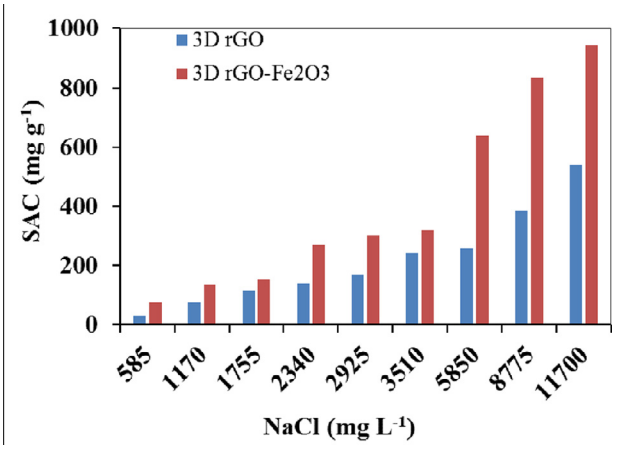

Fig. 12. Electrosorption capacity of 3D rGO and 3D rGO-Fe_2O_3 electrodes at different NaCl concentrations.

of the 3D rGO electrodes at the all concentrations levels, which indicates that more ions were adsorbed in its pores. Therefore, the mostly results verify that the 3D rGO-Fe_2O_3 material is a notable candidate for capacitive deionization (Fig. 12).

These results allow to conclude that the new developed hydrothermal synthesis method is able to create 3D rGO structures that involves many macropores for ion immobility and a designed network of mesoporous which contributes high surface area with better transport pathways and gives a guarantee on a large place for ion lodging in CDI process. Besides, the addition of iron oxide nanoparticles between the graphene oxide sheets enhances the wettability and the hydrophilicity of the electrodes allowing higher accessibility to store a great quantity of the salt ions. The role of iron oxide on the high performance of the 3D rGO-Fe_2O_3 could be explained based on the fact that the nanoparticles of Fe_2O_3 synthetized by the hydrothermal method have the presence of surface sites [$FeO_x(OH)_y$] containing OH labile ligands, which confer hydrophilicity and numerous places to interact with the cations and anions from the solution [52–54].

4. Conclusions

A 3D reduced graphene oxide-iron oxide (3D rGO-Fe_2O_3) was successfully synthesised with a specific combination of macropore/mesopore and micropore structure for its use as active material in electrodes for capacitive deionization (CDI). This material shows a high specific capacitance (345.13 F g^{-1} at 5 mV s^{-1}) and high adsorption capacity (945.1 mg g^{-1} for 11,700 mg L^{-1} NaCl solutions) compared

Table 3
Sodium chloride electroadsorption capacity of different materials available in the literature in comparison to 3D rGO-Fe_2O_3 studied in this work.

[NaCl] (mg/L)	This work mg/g	SoA Electrode	mg/g
11,700	945.1	—	—
9570	—	Mesoporous carbon coated graphite with a fibre sheet	7.1 [60]
8766	835.2	—	—
7340	—	Mesoporous carbon coated graphite with a fibre sheet	10.0 [60]
5844	637.4	AC	3.3 [55]
		Graphene aerogel	15.4 [35]
		Graphene aerogel/TiO_2	24.2 [35]
5000	—	3D porous graphene hydrogels	26.8 [56]
4460	—	Mesoporous carbon coated graphite with a fibre sheet	14.5 [60]
3970	—	Mesoporous carbon coated graphite with a fibre sheet	14.6 [60]
2922	301.1	—	—
2000	—	3:1 Reduced graphene oxide/titanium dioxide nanotubes	99.5 [34]
1753	153.9	—	—
1649	—	Granular activated carbon	9.6 [57]
		P-doped carbon nanofiber aerogels	16.2 [58]
1461	—	Carbon black loaded N-doped carbon aerogel	7.3 [59]
1200	136.28	Mesoporous carbon coated graphite with a fibre sheet	6.1 [60]
		Activated carbon	12.1 [61]
1000	—	Carbon nanotubes	15.6 [62]
936	—	Activated carbon fibre	1.6 [63]
600	—	Activated carbon	2.0 [64]
		Activated carbon +Ag (AgPAC)	5.3 [43]
		Multiwalled carbon nanotube	5.3 [43]
585	76.93	Activated carbon cloth	4.0 [65]
		3D porous graphene foams	29.6 [66]
500	—	Ag-doped hollow ZIFs-derived nanoporous carbon	29.2 [67]

with other carbon materials for CDI electrodes presented in the literature. The incorporation of iron oxide nanoparticles was demonstrated to be beneficial to increase the specific capacitance and the specific surface area of 3D rGO, which results in a much higher NaCl uptake in the CDI process. In conclusion, compared to other carbon materials, the as-synthesised 3D rGO/Fe_2O_3 material could be an excellent candidate as electrode for a skilful CDI process in saline water desalination and drinking water purification.

Declaration of Competing Interest

The authors declare no known conflict of interest.

Acknowledgments

This project has received funding from the European Union's Horizon 2020 research and innovation programme Graphene Flagship under grant agreement No 881603.

References

[1] World Health Organization, https://www.who.int/heli/risks/water/water/en/.
[2] M. Elimelech, W.A. Philip, The future of seawater desalination: energy, technology and the environment, Science 333 (2011) 712–717, doi:10.1126/science.1200488.
[3] C.J. Gabelich, T.D. Tran, I.H.M. Suffet, Electrosorption of inorganic salts from aqueous solution using carbon aerogels, Environ. Sci. Technol. 36 (2002) 3010, doi:10.1021/es0112745.
[4] T.J. Welgemoed, C.F. Schutte, Capacitive deionization technology TM: an alternative desalination solution, Desalination 183 (2005) 327, doi:10.1016/j.desal.2005.02.054.
[5] Y. Oren, Capacitive deionization (CDI) for desalination and water treatment — past, present and future (a review), Desalination 22 (2008) 10, doi:10.1016/j.desal.2007.08.005.
[6] M.A. Anderson, A.L. Cudero, J. Palma, Capacitive deionization as an electrochemical means of saving energy and delivering clean water. Comparison to present desalination practices: will it compete? Electrochem. Acta 55 (2010) 3845, doi:10.1016/j.electacta.2010.02.012.
[7] S. Porada, R. Zhao, A. van der Wal, V. Presser, P.M. Biesheuvel, Review on the science and technology of water desalination by capacitive deionization, Prog. Mater. Sci 58 (2013) 1388–1442, doi:10.1016/j.pmatsci.2013.03.005.
[8] A. Hemmatifar, J.W. Palko, M. Stadermann, J.G. Santiago, Energy breakdown in capacitive deionization, Water Res. 104 (2016) 303–311, doi:10.1016/j.watres.2016.08.020.
[9] B.B. Arnold, G.W. Murphy, Studies on the electrochemistry of carbon and chemically modified carbon surfaces, J. Phys. Chem. 65 (1961) 135, doi:10.1021/j100819a038.
[10] B. Jia, L. Zou, Wettability and its influence on graphene nansoheets as electrode material for capacitive deionization, Chem. Phys. Lett. 548 (2012) 23–28, doi:10.1016/j.cplett.2012.06.016.
[11] S.S. Gupta, M.R. Islam, T. Pradeep, Capacitive deionization (CDI): an alternative cost-efficient desalination technique, Adv. Water Purif. Tech. (2019) 165–202, doi:10.1016/B978-0-12-814790-0.00007-7.
[12] Y.M. Volfkovich, Capacitive deionization of water (A review), Russ. J. Electrochem. 56 (1) (2020) 20–55, doi:10.1134/S1023193520010097.
[13] Y. Liu, Ch. Nie, X. Liu, X. Xu, Z. Sun, L. Pan, Review on carbon-based composite materials for capacitive deionization, RSC Adv. 5 (2015) 15205–15225, doi:10.1039/c4ra14447c.
[14] F. Al Suwaidi, H. Younes, V. Sreepal, R.R. Nair, C. Aubry, L. Zou, Strategies for tuning hierarchical porosity of 3D rGO to optimize ion electrosorption, 2D Mater. 6 (2019) 045010, doi:10.1088/2053-1583/ab2927.
[15] F.A. Almarzooqi, A.A. Al Ghaferi, I. Saadat, N. Hilal, Application of capacitive deionisation in water desalination: a review, Desalination 342 (2014) 3–15, doi:10.1016/j.desal.2014.02.031.
[16] L.T.N. Huynh, T.N. Pham, T.H. Nguyen, V.H. Le, T.T. Nguyen, T.D.K. Nguyen, T.N. Tran, P.A.V. Ho, T.T. Co, T.T.T. Nguyen, T.K.A. Vo, T.H. Nguyen, T.T. Vu, V.M. Luong, H. Uyama, G.V. Pham, T. Hoang, D.L. Tran, Coconut shell-derived activated carbon and carbon nanotubes composite: a promising candidate for capacitive deionization electrode, Synth. Met. 265 (2020) 11641, doi:10.1016/j.synthmet.2020.116415.
[17] O. Sufiani, H. Tanaka, K. Teshima, R.L. Machunda, Y.A.C. Jande, Enhanced electrosorption capacity of activated carbon electrodes for deionized water production through capacitive deionization, Sep. Purif. Technol. 247 (2020) 116998, doi:10.1016/j.seppur.2020.116998.
[18] N. Linneen, F. Delnick, S.Z. Islam, V.G. Deshmane, R. Bhave, Application of the macrohomogeneous line model for the characterization of carbon aerogel electrodes in capacitive deionization, Electrochim. Acta 301 (2019) 1–7 0013-4686, doi:10.1016/j.electacta.2019.01.123.
[19] Y. Liu, T. Chen, T. Lu, Z. Sun, D.H.C. Chua, L. Pan, Nitrogen-doped electrospun reduced graphene oxide-carbon nanofiber composite for capacitive deionization, RSC Adv. 5 (2015) 34117–34124, doi:10.1016/j.electacta.2015.01.179.
[20] M. Mengjuan, L. Xiaojun, K. Weiqing, G. Yongjie, D. Weiqi, H. Jiawen, Hierarchical composite of N-doped carbon sphere and holey graphene hydrogel for high-performance capacitive deionization, Desalination 464 (2019) 18–24, doi:10.1016/j.desal.2019.04.014.
[21] J. Li, B. Ji, R. Jiang, P. Zhang, N. Chen, G. Zhang, L. Qu, Hierarchical hole enhanced 3D graphene assembly for highly efficient capacitive deionization, Carbon 129 (2018) 95–103, doi:10.1016/j.carbon.2017.11.095.
[22] S. Porada, L. Borchardt, M. Oschatz, M. Bryjak, J.S. Atchison, K.J. Keesman, S. Kaskel, P.M. Biesheuvel, V. Presser, Direct prediction of the desalination performance of porous carbon electrodes for capacitive deionization, Energy Environ. Sci. 6 (2013) 3700–3712, doi:10.1039/C3EE42209G.

[23] B. Han, G. Cheng, Y. Wang, X. Wang, Structure and functionality design of novel carbon and faradaic electrode materials for high-performance capacitive deionization, Chem. Eng. J. 360 (2019) 364–384, doi:10.1016/j.cej.2018.11.236.

[24] S.Y. Ahmed, O.M. Hend, M.A.M. Ibrahim, M.M. Hamouda, A.M.B. Nasser, Enhanced desalination performance of capacitive deionization using zirconium oxide nanoparticles-doped graphene oxide as a novel and effective electrode, Sep. Purif. Technol. 171 (2016) 34–43, doi:10.1016/j.seppur.2016.07.014.

[25] C. Zhao, X. Wang, S. Zhang, N. Sun, H. Zhou, G. Wang, Y. Zhang, H. Zhang, H. Zhao, Porous carbon nanosheets functionalized with Fe_3O_4 nanoparticles for capacitive removal of heavy metal ions from water, Environ. Sci. Water Res. Technol. 6 (2020) 331, doi:10.1039/c9ew00472f.

[26] Y. Cheng, Z. Hao, C. Hao, Y. Deng, X. Li, K. Li, Y. Zhao, A review of modification of carbon electrode material in capacitive deionization, J. RSC Adv. 9 (2019) 24401, doi:10.1039/c9ra04426d.

[27] K. Jo, Y. Baek, C. Lee, J. Yoon, Effect of hydrophilicity of activated carbon electrodes on desalination performance in membrane capacitive deionization, Appl. Sci. 9 (2019) 5055, doi:10.3390/app9235055.

[28] Y. Wang, L. Guo, P. Qi, X. Liu, G. Wei, Synthesis of three-dimensional graphene-based hybrid materials for water purification: a review, Nanomaterials 9 (2019) 1123, doi:10.3390/nano9081123.

[29] K.C. Leonard, J.R. Genthe, J.L. Sanfilippo, W.A. Zeltner, M.A. Anderson, Synthesis and characterization of asymmetric electrochemical capacitive deionization materials using nanoporous silicon dioxide and magnesium doped aluminum oxide, Electrochim. Acta 54 (2009) 5286–5291, doi:10.1016/j.electacta.2009.01.082.

[30] P.Ho Kim, K.Y. Jung, A new strategy of spray pyrolysis to prepare porous carbon nanosheets with enhanced ionic sorption capacity, RSC Adv. 6 (2016) 1686–1693, doi:10.1039/c5ra23785h.

[31] H. Li, Z.Y. Leong, W. Shi, J. Zhang, T. Chen, H.Y. Yang, Hydrothermally synthesized graphene and Fe_3O_4 nanocomposites for high performance capacitive deionization, RSC Adv. 6 (2016) 11967, doi:10.1039/c5ra23151e.

[32] J. Wu, X. Shen, L. Jiang, K. Wang, K. Chen, Solvothermal synthesis and characterization of sandwich-like graphene/ZnO nanocomposites, Appl. Surf. Sci. 256 (2010) 2826–2830, doi:10.1016/j.apsusc.2009.11.034.

[33] Y. Liu, L. Pan, T. Chen, X. Xu, T. Lu, Z. Sun, D.H.C. Chua, Porous carbon spheres via microwave-assisted synthesis for capacitive deionization, Electrochim. Acta 151 (2015) 489–496, doi:10.1016/j.electacta.2014.11.086.

[34] X.J. Zhang, G.S. Wang, W.Q. Cao, Y.Z. Wei, J.F. Liang, L. Guo, M.S. Cao, Enhanced microwave absorption property of reduced graphene oxide (RGO)-$MnFe_2O_4$ nanocomposites and polyvinylidene fluoride, ACS Appl. Mater. Interfaces 6 (2014) 7471–7478, doi:10.1021/am500862g.

[35] M.E. Suss, T.F. Baumann, W.L. Bourcier, C.M. Spadaccini, K.A. Rose, J.G. Santiago, M. Stadermann, Capacitive desalination with flow-through electrodes, Energy Environ. Sci. 5 (2012) 9511–9519, doi:10.1039/c2ee21498a.

[36] A. Bahramia, I. Kazeminezhada, Y. Abdic, Pt-Ni/rGO counter electrode: electrocatalytic activity for dye sensitized solar cell, Superlattices Microstruct. 125 (2019) 125–137, doi:10.1016/j.spmi.2018.10.026.

[37] J. Ma, L. Wang, F. Yu, X. Dai, Mesoporous amorphous $FePO_4$ nanosphere@Graphene as a faradic electrode in capacitive deionization for high-capacity and fast removal of NaCl from wáter, Chem. Eng. J. 370 (2019) 938–943, doi:10.1016/j.cej.2019.03.243.

[38] X. Wu, Study of sintered ceramic process based on thermal analysis, in: Proceedings of the 4th International Conference on Mechanical Materials and Manufacturing Engineering (MMME, 2016.

[39] A. Eckmann, A. Felten, A. Mishchenko, L. Britnell, R. Krupke, K.S. Novoselov, C. Casiraghi, Probing the nature of defects in graphene by Raman spectroscopy, Nano Lett. 12 (8) (2012) 3925–3930, doi:10.1021/nl300901a.

[40] Y. Li, I. Hussain, J. Qi, Ch. Liu, J. Li, J. Shen, X. Sun, W. Han, L. Wang, N-doped hierarchical porous carbon derived from hypercrosslinked diblock copolymer for capacitive deionization, Sep. Purif. Technol. 165 (2016) 190–198, doi:10.1016/j.seppur.2016.04.007.

[41] M. Thommes, Physical adsorption characterization of nanoporous materials, Chem. Ing. Tech. 82 (2010) 1059–1073, doi:10.1002/cite.201000064.

[42] W. Huang, Y. Zhang, S. Bao, S. Song, Desalination by capacitive deionization with carbon-based materials as electrode: a review, Surf. Rev. Lett. 20 (10p) (2013) 1330003, doi:10.1142/S0218625x13300050.

[43] T. Tsoncheva, J. Rosenholm, M. Linden, F. Kleitz, M. Tiemann, L. Ivanova, M. Dimitrov, D. Paneva, I. Mitov, C. Minchev, Critical evaluation of the state of iron oxide nanoparticles on different mesoporous silicas prepared by an impregnation method, Microporous Mesoporous Mater. 112 (2008) 327–337, doi:10.1016/j.micromeso.2007.10.005.

[44] R.L. Zornitta, J.J. Lado, M.A. Anderson, L.A.M. Ruotolo, Effect of electrode properties and operational parameters on capacitive deionization using low-cost commercial carbons, Sep. Purif. Technol. 158 (2016) 39–52, doi:10.1016/j.seppur.2015.11.043.

[45] M. Vujkovic, N. Gavrilov, I. Pasti, J. Krstic, J. Travas-Sejdic, G. Ciric-Marjanovic, S. Mentus, Superior capacitive and electrocatalytic properties of carbonized nanostructured polyaniline upon a low-temperature hydrothermal treatment, Carbon 64 (2013) 472–486, doi:10.1016/j.carbon.2013.07.100.

[46] S.J. Seo, H. Jeon, J.K. Lee, G.Y. Kim, D. Park, H. Nojima, J. Lee, S.H. Moon, Investigation on removal of hardness ions by capacitive deionization (CDI) for water softening applications, Water Res. 44 (2010) 2267–2275, doi:10.1016/j.watres.2009.10.020.

[47] A.S. Yasin, H.O. Mohamed, I.M.A. Mohamed, H.M. Mousa, N.A.M. Barakat, Enhanced desalination performance of capacitive deionization using zirconium oxide nanoparticles-doped graphene oxide as a novel and effective electrode, Sep. Purif. Technol. 171 (2016) 34–43 1383-5866, doi:10.1016/j.seppur.2016.07.014.

[48] C. Kim, B.T.N. Ngoc, K.S. Yang, M. Kojima, Y.A. Kim, Y.J. Kim, M. Endo, S.C. Yang, Self-sustained thin webs consisting of porous carbon nanofibers for supercapacitors via the electrospinning of polyacrylonitrile solutions containing zinc chloride, Adv. Mater. 19 (2007) 2341–2346, doi:10.1002/adma.200602184.

[49] X. Xu, Z. Sun, D.H.C. Chua, L. Pan, Novel nitrogen doped graphene sponge with ultrahigh capacitive deionization performance, Sci. Rep. 5 (2015) 11225, doi:10.1038/srep11225.

[50] J. Han, L. Shi, T. Yan, J. Zhang, D. Zhang, Removal of ions from saline water using N, P codoped 3D hierarchical carbon architectures via capacitive deionization, Environ. Sci. Nano 5 (2018) 2337, doi:10.1039/C8EN00625K.

[51] M. Noked, E. Avraham, A. Soffer, D. Aurbach, The rate-determining step of electroadsorption processes into nanoporous carbon electrodes related to water desalination, J. Phys. Chem. C 113 (2009) 21319–21327, doi:10.1021/jp905987j.

[52] S. Chatman, P. Zarzycki, K.M. Rosso, Surface potentials of (001), (012), (113) hematite (α-Fe_2O_3) crystal faces in aqueous solution, Phys. Chem. 15 (2013) 13911–13921, doi:10.1039/c3cp52592a.

[53] H. Hohl, L. Sigg, W. Stumm, Characterization of surface chemical properties of oxides in natural waters, The Role of Specific Adsorption in Determining the Surface Charge, Advances in Chemistry, American Chemical Society, Washington, DC, 1980, doi:10.1021/ba-1980-0189.ch001.

[54] P.S. Pinto, T.P.V. Medeiros, J.D. Ardisson, R.M. Lago, Role of [FeOx(OH)y] surface sites on the adsorption of β-lactamic antibiotics on Al_2O_3 supported Fe oxide, J. Hazard. Mater. 317 (2016) 327–384, doi:10.1016/j.jhazmat.2016.05095.

[55] H. Yin, S. Zhao, J. Wan, H. Tang, L. Chang, L. He, H. Zhao, Y. Gao, Z. Tang, Three-dimensional graphene/metal oxide nanoparticle hybrids for high-performance capacitive deionization of saline water, Adv. Mater. 25 (2013) 6270–6276, doi:10.1002/adma.201302223.

[56] W. Kong, X. Duan, Y. Ge, H. Liu, J. Hu, X. Duan, Holey graphene hydrogel with in-plane pores for high performance capacitive desalination, Nano Res. 9 (8) (2016) 2458–2466, doi:10.1007/s12274-016-1132-8.

[57] Z. Sun, L. Chai, M. Liu, Y. Shu, Q. Li, Y. Wang, Q. Wang, D. Qiu, Capacitive deionization of chloride ions by activated carbon using a three-dimensional electrode reactor, Sep. Purif. Technol. 191 (2018) 424–432, doi:10.1016/j.seppur.2017.09.015.

[58] P.I. Liu, L.C. Chung, C.H. Ho, H. Shao, T.M. Liang, M.C. Chang, C.C.M. Ma, R.Y. Horng, Comparative insight into the capacitive deionization behavior of the activated carbon electrodes by two electrochemical techniques, Desalination 379 (2016) 34–41, doi:10.1016/j.desal.2015.10.008.

[59] G. Rasines, P. Lavela, C. Macías, M.C. Zafra, J. L.Tirado, C.O. Ania, On the use of carbon black loaded nitrogen-doped carbon aerogel for the electrosorption of sodium chloride from saline water, Electrochim. Acta 170 (2015) 154–163 1016/j.electacta.2015.04.137.

[60] C. Tsouris, R. Mayes, J. Kiggans, K. Sharma, S. Yiacoumi, D. DePaoli, S. Dai, Mesoporous carbon for capacitive deionization of saline water, Environ. Sci. Technol. 45 (2011) 10243–10249, doi:10.1021/es201551e.

[61] P.I. Liu, L.C. Chung, C.H. Ho, H. Shao, T.M. Liang, M.C. Chang, C.C.M. Ma, R.Y. Horng, Comparative insight into the capacitive deionization behavior of the activated carbon electrodes by two electrochemical techniques, Desalination 379 (2016) 34–41, doi:10.1016/j.desal.2015.10.008.

[62] J. Xie, J. Ma, L. Wu, M. Xu, W. Ni, Y.M. Yan, Carbon nanotubes in-situ cross-linking the activated carbon electrode for high-performance capacitive deionization, Sep. Purif. Technol. 239 (2020) 116593, doi:10.1016/j.seppur.2020.116593.

[63] Z.H. Huang, J. Wang, C. Zhang, F. Kang, Relation between the charge efficiency of activated carbon fiber and its desalination performance, Langmuir 28 (2012) 5079–5084, doi:10.1021/la204690s.

[64] T. Alencherry, A.R. Naveen, G. Somnath, D. Jency, R. Venkataraghavan, Effect of increasing electrical conductivity and hydrophilicity on the electrosorption capacity of activated carbon electrodes for capacitive deionization, Desalination 415 (2017) 14–19, doi:10.1016/j.desal.2017.04.001.

[65] L. Agartan, B. Akuzum, T. Mathis, K. Ergenekon, E. Agar, E.C. Kumbur, Influence of thermal treatment conditions on capacitive deionization performance and charge efficiency of carbon electrodes, Sep. Purif. Technol. 202 (2018) 67–75, doi:10.1016/j.seppur.2018.02.039.

[66] J. Li, R. Jiang, P. Zhang, N. Chen, G. Zhang, L. Qu, Hierarchical hole-enhanced 3D graphene assembly for highly efficient capacitive deionization, Carbon 129 (2018) 95–103, doi:10.1016/j.carbon.2017.11.095.

[67] H. Zhang, W. Zhang, J. Shen, Y. Li, X. Yan, J. Qi, X. Sun, J. Shen, W. Han, L. Wang, J. Li, Ag-doped hollow ZIFs-derived nanoporous carbon for efficient hybrid capacitive deionization, Desalination 473 (2020) 114173, doi:10.1016/j.desal.2019.114173.